IEEE Robotics and Automation Letters (RA-L) paper, presented at ICRA 2026, Vienna, Austria. Cite as RA-L paper.

Optimal Design of Integrated Aerial Platforms with Passive Joints

Yushu Yu, Kaidi Wang, Xin Meng, Jianrui Du, Jiali Sun, Ganghua Lai, Yibo Zhang

***Abstract*— The Integrated Aerial Platform (IAP) uses multiple quadrotor sub-vehicles, acting as independent thrust generators, connected to a central platform via passive joints. This setup allows the sub-vehicles to collectively apply forces and torques to the central platform, achieving full six-degree-of-freedom (6-DoF) motion through coordinated thrust and posture adjustments. The IAP's modular design offers significant advantages in terms of mechanical simplicity, reconfigurability for diverse scenarios, and enhanced mission adaptability. This paper presents a comprehensive framework for IAP modeling and optimal design. We introduce a "design matrix" that encapsulates key architectural parameters, including the number of sub-vehicles, their spatial configuration, and the types of passive joints used. To improve control performance and ensure balanced wrench generation capabilities, we propose an optimized design strategy that minimizes the condition number of this design matrix. Two distinct IAP configurations were optimally designed based on two typical application scenarios. The efficacy of the proposed optimization methodology was subsequently validated through comparative analysis against unoptimized platforms. Moreover, the full actuation capability of the IAP was empirically confirmed via extensive simulations and real-world flight experiments, which also demonstrated its operational performance through direct wrench control experiment.**

I. Introduction

Small-scale quadrotors have been extensively studied and utilized across various domains due to their mechanical simplicity, agility, and vertical takeoff and landing capabilities [1]. Applications range from basic remote sensing [2] to more complex interactions with the environment and humans [3]. Small-scale quadrotors have been extensively studied for their mechanical simplicity, agility, and vertical takeoff capabilities, enabling numerous applications in remote sensing and physical interactions with the environment [4]. Early efforts in aerial manipulation often relied on unidirectional-thrust vehicles with collinear rotors, using external tools such as cables [5] or rigid implements [6], [7]. In addition, some studies use combinations of multiple coplanar rotors [8] or quadrotors [9] to accommodate collaborative handling of objects with diverse shapes. However, their under-actuated nature restricting independent 6-DOF wrench generation and added manipulator weight reducing thrust-to-weight ratios remain key challenges.

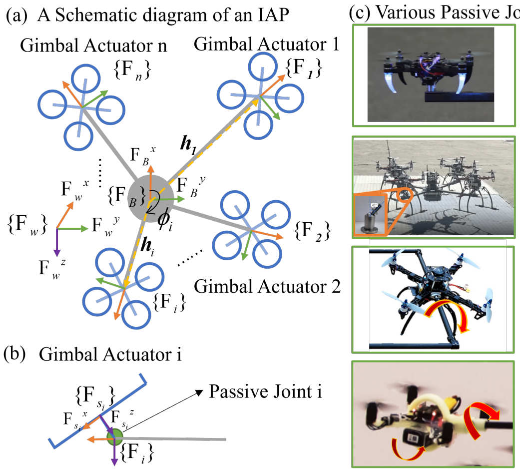

Fig. 1: (a) A schematic diagram of an IAP illustrating its main framework and four of the n universal joint actuators. (b) Each actuator comprises a sub-vehicle and a passive joint. (c) Four types of selectable passive joints are depicted.

Fully actuated aerial platforms, capable of generating a 6D wrench, are categorized into three main types [10]. The first involves multirotor drones with tilted propellers, where at least six propellers are arranged in various directions [11]. The second approach actively tilts the aerial vehicle's propellers using additional actuators [12]. A third class achieves full actuation by integrating multiple under-actuated aerial vehicles through passive joints, including constrained passive joints [13], single-bearing joints [14], [15], double-bearing joints [10], and spherical joints [16], [17].

The IAP falls under the third category of aerial platforms, directly addressing the 6-DoF wrench generation limitation of typical under-actuated vehicles, which is crucial for complex aerial manipulation tasks like drilling and pulling [16], [18]. Compared to other fully actuated platforms, the IAP offers superior energy efficiency by utilizing interconnected under-actuated vehicles instead of complex tilting rotors [19]. Its modular and reconfigurable design allows adaptation to diverse flight scenarios by varying sub-vehicle numbers, arrangements, and passive joint types, enhancing environmental adaptability. However, fundamental design principles for various scenarios, design optimization, and control stability remain largely unexplored.

Optimization design for multi-vehicle platforms has been explored through various approaches. Koshi et al. [8] and Bingguo et al. [7] developed systems where sub-vehicles lack independent flight, and the combined platforms is under-

This work was supported by the National Natural Science Foundation of China under Grant 62173037, National Key R. D. Program of China, State Key Laboratory of Robotics and Systems (HIT), and Beijing Institute of Technology Research Fund Program for Young Scholars. (*Corresponding author: Yushu Yu, Yibo Zhang)*

Yushu Yu, Kaidi Wang, Jianrui Du, Jiali Sun, Ganghua Lai, and Yibo Zhang are with the School of Mechatronical Engineering, Beijing Institute of Technology, Beijing 100081, China. (e-mail: yushu.yu@bit.edu.cn)

Xin Meng is with the Department of Mechanical Engineering, National University of Singapore, Singapore. (e-mail: mengxin@nus.edu.sg)

actuated. Similarly, Carlo et al. [9] optimized a quadcopter-based cooperative system, but its rigid sub-unit connection also precluded full actuation. Other research includes Yao Su et al.'s genetic algorithm-based modular UAV flight structure optimization [20], Vijay Kumar et al.'s virtual kinematic chain approach for drone operation platforms [21], and Jianrui Du et al.'s modular simulator for IAPs supporting diverse configurations [22]. A common limitation across these studies is the consideration of only uniform joint types or simplified kinematic assumptions, neglecting scenarios with diverse passive joint linkages between modular sub-vehicles.

The optimal design of IAP with passive joints presents several unsolved challenges. First, previous studies have primarily used the identical type of passive joints for IAP sub-vehicles, leaving a gap in research on IAP systems that combine multiple types of passive joints. Second, existing optimization algorithms, which treat the system's full actuation condition as a constraint, are insufficient for handling the complexity of IAP designs involving diverse passive joint combinations. Finally, current research lacks experimental validation for IAP systems employing different types of passive joints.

This paper presents a modeling and optimization framework for the design of IAP systems with various passive joint types. Overall, the contribution of the paper is summarized as:

- To systematically parameterize the IAP model, we introduce the concept of *design matrix*, which encapsulates critical structural information, including the number of IAP sub-vehicles, their mounting positions, and joint types.
- We propose an optimization method that targets platform-level configuration, independent of sub-vehicles internal actuation, and tunes the design matrix to achieve fully actuated configurations under varying operational constraints.
- Two case studies are presented to illustrate the approach, where control strategies are developed, and the fully actuated capability of the resulting designs is validated through simulations and real-world flight experiments.

II. MODELING OF IAP SYSTEMS

The IAP has a modular design consisting of sub-vehicles, a central platform, connection rods, and passive joints. All sub-vehicles are quadrotors, which only generate thrust normal to their rotor plane and 3-axis torques. As shown in Fig. 1-(a), the sub-vehicles are connected to the central platform via passive joints and connection rods, forming a star configuration. Let n denote the total number of sub-vehicles. Each gimbal actuator, indexed as i where $i \in \{1, \ldots, n\}$, as shown in Fig. 1-(b), represents a unit that generates a wrench. This unit consist of a sub-vehicle and a passive joint. Notably, each gimbal actuator may be equipped with different types of passive joints. Fig. 1-(c) shows four commonly used passive joint types: fixed, spherical, single-bearing, and double-bearing.

A. Coordinate Frames and Transformations

The world coordinate system $\mathcal{F}_w = \{O_w, \mathcal{F}_w^x, \mathcal{F}_w^y, \mathcal{F}_w^z\}$ is defined with an arbitrary origin O_w. Its axes are oriented as follows: $\mathcal{F}_w^x$ points north, $\mathcal{F}_w^y$ points east, and $\mathcal{F}_w^z$ points downward, aligned with gravitational acceleration $g = 9.8\,\mathrm{m/s}^2$.

The IAP body frame, denoted as $\mathcal{F}_B = \{O_B, \mathcal{F}_B^x, \mathcal{F}_B^y, \mathcal{F}_B^z\}$, is rigidly attached to the IAP central platform. Its origin O_B is set at the central platform's center of mass (CoM), where the x-axis $\mathcal{F}_B^x$ aligns with the platform's forward direction, the y-axis $\mathcal{F}_B^y$ points to the right, and the z-axis $\mathcal{F}_B^z$ points downward.

Each sub-vehicle is associated with a local coordinate frame $\mathcal{F}_{Bi} = \{O_{Bi}, \mathcal{F}_{Bi}^x, \mathcal{F}_{Bi}^y, \mathcal{F}_{Bi}^z\}$. The origin O_{Bi} is set at the rotational center of the passive joint (spherical joint or bearing joint) or the constrained passive joint. The frame $\{\mathcal{F}_{Bi}\}$ is obtained by rotating $\{\mathcal{F}_B\}$ around the z-axis $\mathcal{F}_B^z$ by an angle ϕ_i. Assuming each sub-vehicle is initially installed in a plane parallel to the central platform, the transformation between the frames $\{\mathcal{F}_{Bi}\}$ and $\{\mathcal{F}_B\}$ is defined by $(\mathbf{R}_{Bi}^B, \mathbf{h}_i)$, where $\mathbf{h}_i = [h_i^x, h_i^y, h_i^z]^T \in \mathbb{R}^3$ denotes the displacement from O_B to O_{Bi}, and $\mathbf{R}_{Bi}^B \in \mathbb{R}^{3\times3}$ represents the corresponding rotation:

$$\mathbf{R}_{Bi}^B = \begin{bmatrix} \cos\phi_i & -\sin\phi_i & 0 \\ \sin\phi_i & \cos\phi_i & 0 \\ 0 & 0 & 1 \end{bmatrix}. \tag{1}$$

As shown in Fig. 1-(b), the sub-vehicle body frame $\{\mathcal{F}_{si}\}$ is attached to the CoM of each sub-vehicle. For optimal structural design, its origin O_{si} should be positioned as close as possible to the rotation center or axis of its corresponding passive joint, which is mounted at the end of the central platform's connection rod.

B. IAP Dynamics

We model the IAP as a rigid body with mass $m \in \mathbb{R}$ and a positive definite moment of inertia matrix $\mathbf{J} \in \mathbb{R}^{3\times3}$, defined relative to the central platform's CoM at O_B [16]. The system's dynamics are formulated using the Newton-Euler equations, as follows:

$$\mathbf{M}_B\dot{\mathbf{V}}_B + \mathbf{C}_B\mathbf{V}_B + \mathbf{G}_B = \begin{bmatrix} \mathbf{R}_B^W & \mathbf{0} \\ \mathbf{0} & \mathbf{I}_{3\times3} \end{bmatrix}\mathbf{W}, \tag{2}$$

where $\mathbf{M}_B \in \mathbb{R}^{6\times6}$, $\mathbf{C}_B \in \mathbb{R}^{6\times6}$, and $\mathbf{G}_B \in \mathbb{R}^6$ represent the mass matrix, Coriolis matrix, and gravity matrix, respectively:

$$\begin{aligned} \mathbf{M}_B &= \begin{bmatrix} m\mathbf{I}_{3\times3} & \mathbf{0} \\ \mathbf{0} & \mathbf{J} \end{bmatrix}, \quad \mathbf{C}_B = \begin{bmatrix} \mathbf{0} & \mathbf{0} \\ \mathbf{0} & -\mathbf{\Omega}_B \end{bmatrix}, \\ \mathbf{G}_B &= \begin{bmatrix} mg\mathbf{e}_3 \\ \mathbf{h}_0^\wedge mg\mathbf{e} \end{bmatrix}, \end{aligned} \tag{3}$$

where $\mathbf{e}_3 = [0,0,1]^T$ is the unit vector, $\mathbf{I}_{3\times3} \in \mathbb{R}^{3\times3}$ is the identity matrix, and $\mathbf{\Omega}_B = (\mathbf{J}\boldsymbol{\omega}_B)^\wedge$ is the skew symmetric matrix encoding the cross-product operation for the angular momentum $\mathbf{J}\boldsymbol{\omega}_B$. And $\mathbf{V}_B = [\boldsymbol{v}_B; \boldsymbol{\omega}_B] \in \mathbb{R}^6$ represents the velocity of the IAP's CoM, where $\boldsymbol{v}_B \in \mathbb{R}^3$ is the linear velocity, expressed in frame $\{\mathcal{F}_W\}$, and $\boldsymbol{\omega}_B \in \mathbb{R}^3$ is the angular velocity, expressed in frame $\{\mathcal{F}_B\}$. $\mathbf{h}_0 \in \mathbb{R}^3$ is the vector from O_B to the full system CoM expressed in $\{\mathcal{F}_B\}$, which is the weighted average of the central platform and sub-vehicles' CoM. The matrix $\mathbf{R}_B^W \in SO(3)$ represents the orientation of $\{\mathcal{F}_B\}$ relative to $\{\mathcal{F}_W\}$. $\mathbf{W} = [\boldsymbol{f}_B; \boldsymbol{\tau}_B] \in \mathbb{R}^6$ represents the total controllable wrench applied to the central platform, where $\boldsymbol{f}_B, \boldsymbol{\tau}_B \in \mathbb{R}^3$ denote the net force and torque, respectively, both expressed in $\{\mathcal{F}_B\}$.

C. Wrench Allocation

In the IAP with n gimbal actuators, each actuator generates a force vector $\boldsymbol{f}_i^B \in \mathbb{R}^3$ and a torque vector $\boldsymbol{\tau}_i^B \in \mathbb{R}^3$, both defined in the frame $\{\mathcal{F}_B\}$. These forces and torques contribute to form the total controllable input force f_B and torque $\boldsymbol{\tau}_B$.

The wrench produced by each gimbal actuator i is represented as $\mathbf{W}_i^B = [\boldsymbol{f}_i^B; \boldsymbol{\tau}_i^B] \in \mathbb{R}^6$. Thus, the total controllable wrench is given by the sum of all actuator wrenches $\mathbf{W} = \sum_{i=1}^n \mathbf{B}_i \mathbf{W}_i^B$, where $\mathbf{B}_i = [\mathbf{B}_{fi}; \mathbf{B}_{\tau i}] \in \mathbb{R}^{6\times 6}$ is the transformation matrix that maps the individual actuator wrenches to the total platform wrench. The submatrices are defined as $\mathbf{B}_{f_i} = [\mathbf{I}_{3\times 3}\ \mathbf{0}_{3\times 3}] \in \mathbb{R}^{3\times 6}$ and $\mathbf{B}_{\tau_i} = [\mathbf{h}_i\ \mathbf{I}_{3\times 3}] \in \mathbb{R}^{3\times 6}$.

By stacking all actuator wrenches into a single vector $\mathbf{W}_d^B = [\mathbf{W}_1^{B^T} \ldots \mathbf{W}_n^{B^T}]^T \in \mathbb{R}^{6n}$, we can write the total wrench in matrix form as:

$$\mathbf{W} = \mathbf{B}\mathbf{W}_d^B, \tag{4}$$

where, $\mathbf{B} = [\mathbf{B}_1 \ldots \mathbf{B}_n] \in \mathbb{R}^{6\times 6n}$ is the wrench allocation matrix, composed of two sub-matrices: $\mathbf{B} = [\mathbf{B}_f^T, \mathbf{B}_\tau^T]^T$. $\mathbf{B}_f \in \mathbb{R}^{3\times 6n}$ and $\mathbf{B}_\tau \in \mathbb{R}^{3\times 6n}$ are referred to as the force allocation matrix and torque allocation matrix, respectively:

$$\mathbf{B}_f = [\ \mathbf{B}_{f_1} \quad \ldots \quad \mathbf{B}_{f_n}],\ \mathbf{B}_\tau = [\ \mathbf{B}_{\tau_1} \quad \ldots \quad \mathbf{B}_{\tau_n}]. \tag{5}$$

D. Design Matrix Formulation

In an IAP system with passive joints, the force $\boldsymbol{f}_i^{Bi}$ and torque $\boldsymbol{\tau}_i^{Bi}$ generated by the gimbal actuator i are constrained in specific dimensions within the local coordinate system $\{\mathcal{F}_{Bi}\}$. These constraints prevent force or torque generation in certain directions. For example, in a constrained passive joint, forces along the $\mathcal{F}_{Bi}^x$ and $\mathcal{F}_{Bi}^y$ axes cannot be generated, while in a spherical joint, no torques can be generated in any direction in $\{\mathcal{F}_{Bi}\}$.

To systematically incorporate these constraints into the dynamic equations, we define the joint matrix of the gimbal actuator $\mathbf{A}_i \in \mathbb{R}^{6\times 6}$, which encodes the force and torque decoupling as:

$$\mathbf{A}_i = \mathrm{diag}(\alpha_i^1, \alpha_i^2, 1, \beta_i^1, \beta_i^2, \beta_i^3), \tag{6}$$

where $\mathbf{f}_i^\alpha$ represents the force constraints and $\boldsymbol{\tau}_i^\beta$ represents the torque constraints. Specifically, $\mathbf{f}_i^\alpha = [\alpha_i^1\ \alpha_i^2\ 1]^T \in \mathbb{R}^3$ and $\boldsymbol{\tau}_i^\beta = [\beta_i^1\ \beta_i^2\ \beta_i^3]^T \in \mathbb{R}^3$ with $\alpha_i^1, \alpha_i^2 \in \{0,1\}$ and $\beta_i^1, \beta_i^2, \beta_i^3 \in \{0,1\}$. Four general types of passive joint, which will be considered in our design, are associated with a specific $\mathbf{A}_i$, as listed in Table I.

The wrench applied by gimbal actuator i in $\{\mathcal{F}_{Bi}\}$ is $\mathbf{W}_i^{Bi} = [\boldsymbol{f}_i^{Bi}; \boldsymbol{\tau}_i^{Bi}] \in \mathbb{R}^6$. To transform it into the body frame $\{\mathcal{F}_B\}$, we use the joint matrix $\mathbf{A}_i$ and the rotation matrix $\mathbf{R}_{Bi}^B$:

$$\mathbf{W}_i^B = \mathbf{R}_{Bi}^B \mathbf{A}_i \mathbf{W}_i^{Bi}, \tag{7}$$

where $\mathbf{A}_i$ enforces force or torque constraints in specified directions.

Stacking all actuator wrenches from all local frames into a control wrench vector $\mathbf{W}_d^{B1:Bn} = [\mathbf{W}_1^{B1^T} \ldots \mathbf{W}_n^{Bn^T}]^T \in \mathbb{R}^{6n}$, we obtain the relationships between the control wrenches in local frames and the body frame:

$$\mathbf{W}_d^B = \mathbf{R}\mathbf{A}\mathbf{W}_d^{B1:Bn} \tag{8}$$

where $\mathbf{R} = (\mathbf{R}_1, \ldots, \mathbf{R}_n) \in \mathbb{R}^{6n\times 6n}$ is the IAP rotation configuration matrix, $\mathbf{A} = \mathrm{diag}(\mathbf{A}_1, \ldots, \mathbf{A}_n) \in \mathbb{R}^{6n\times 6n}$ is the IAP joint matrix. Each $\mathbf{R}_i$ is defined as:

$$\mathbf{R}_i = \begin{bmatrix} \mathbf{R}_{Bi}^B & \mathbf{0} \\ \mathbf{0} & \mathbf{R}_{Bi}^B \end{bmatrix}. \tag{9}$$

TABLE I: Joint Matrix Elements and Allowed Degrees of Freedom for Different Passive Joints

Joint Type	**Force DoFs ($\mathbf{f}_i$)**	**Torque DoFs ($\boldsymbol{\tau}_i^\beta$)**
Constrained Passive Joint	1 ($[0;0;1]$)	3 ($[1;1;1]$)
Single-Bearing Joint	2 ($[0;1;1]$)	2 ($[0;1;1]$)
Double-Bearing Joint	3 ($[1;1;1]$)	1 ($[0;0;1]$)
Spherical Hinge Joint	3 ($[1;1;1]$)	0 ($[0;0;0]$)

By substituting this transformation into (4) and replacing $\mathbf{W}_d^B$ using (8), we obtain:

$$\mathbf{W} = \begin{bmatrix} \boldsymbol{f}_B \\ \boldsymbol{\tau}_B \end{bmatrix} = \mathbf{B}\mathbf{R}\mathbf{A}\mathbf{W}_d^{B1:Bn}, \tag{10}$$

defining the IAP *design matrix* as $\mathbf{D} = \mathbf{B}\mathbf{R}\mathbf{A} \in \mathbb{R}^{6\times 6n}$, we arrive at the final form:

$$\mathbf{W} = \mathbf{D}\mathbf{W}_d^{B1:Bn}. \tag{11}$$

The *design matrix* $\mathbf{D}$ encapsulates the complete actuation model of IAP, incorporating actuator force and torque generation capabilities, passive joint constraints, and frame transformations. It enables optimization-based joint selection and IAP design.

E. Necessary Condition For Fully Actuated IAP Design

To determine whether an IAP is capable of full actuation, we examine the rank properties of its *design matrix* $\mathbf{D}$. Given the system equation (11), a solution $\mathbf{W}_d^{B1:Bn} \in \mathbb{R}^{6n}$ exists for an arbitrary $\mathbf{W}$ if and only if $\mathbf{D}$ has full row rank. This leads to the following necessary condition:

$$\mathrm{rank}(\mathbf{D}) = 6. \tag{12}$$

This condition is essential for the IAP to be fully actuated; if $\mathrm{rank}(\mathbf{D}) < 6$, the system becomes under-actuated as certain degrees of freedom cannot be independently controlled. In practical applications, sub-vehicle types and flight performance are typically predefined. Consequently, the configuration of the design matrix $\mathbf{D}$ is directly determined by the arrangement of its actuators, specifically their number, positions, orientations, and passive joint types. This leads to the following definition:

Definition 1: IAP design is characterized by the tuple $\mathbb{D} = (n, \mathbf{h}_1, \ldots, \mathbf{h}_n, \phi_1, \ldots, \phi_n, \alpha_1, \beta_1, \ldots, \alpha_n, \beta_n)$, which specifies the number of gimbal actuators n, their positions and orientations relative to $\{\mathcal{F}_B\}$, and the type of passive joint for each actuator. Each tuple $\mathbb{D}$ corresponds to a specific design matrix $\mathbf{D}$.

Definition 2: If the design tuple $\mathbb{D}$ ensures the IAP satisfies (12), let the design tuple $\mathbb{D}_+$ denote the *full actuation design* of the IAP.

III. OPTIMAL DESIGN OF FULLY ACTUATED IAP

A. Optimization Design Problem

A well-conditioned *design matrix* $\mathbf{D} \in \mathbb{R}^{6\times 6n}$ is vital for ensuring that small changes in the control input $\mathbf{W} \in \mathbb{R}^6$ yield minimal deviations in actuator outputs $\mathbf{W}_d^{B1:Bn} \in \mathbb{R}^{6n}$. Poorly conditioned matrices amplify disturbances and numerical errors, leading to degraded control performance.

The numerical stability and robustness of the IAP system are intrinsically linked to the condition number, $\text{cond}(\mathbf{D})$, of its design matrix $\mathbf{D}$. Since a high condition number denotes heightened sensitivity to small perturbations and disturbances, thereby reducing actuation reliability, our objective is to minimize it, leading to the following optimization problem:

Problem 1:

$$\begin{aligned} &\min_{n, \mathbf{h}_i, \phi_i, \alpha_i, \beta_i} && \text{cond}(\mathbf{D}) && (13) \\ &\text{subject to} && \text{rank}(\mathbf{D}) = 6 && (14) \\ & && N_{min} \le n \le N_{max} && (15) \\ & && l_{min} \le l_c \le l_{max} && (16) \end{aligned}$$

Constraints (14) ensures the stability, and efficiency of our numerical optimization algorithm by avoiding singularities, while (15) and (16) enforce mechanical feasibility. $N_{min}, N_{max} \in \mathbb{Z}^+$ bound the count of the gimbal actuators n. For IAP $N_{min} = 2$ and N_{max} is scenario-dependent. The connection rod length $l_c \in \mathbb{R}^+$ is constrained by $l_{min} \in \mathbb{R}^+$ and $l_{max} \in \mathbb{R}^+$, where l_{min} is typically greater than half the wheelbases of the sub-vehicles, and l_{max} is application-dependent. In particular, for operations conducted within confined spaces, l_{max} can be reduced to accommodate prevailing spatial constraints.

B. Algorithm

This section delineates the solution methodology for optimizing the condition number of the design matrix $\mathbf{D}$, as formulated in Problem 1.

The design matrix $\mathbf{D} \in \mathbb{R}^{6\times 6n}$ depends on four critical sets of parameters, including the number of gimbal actuators $n \in \mathbb{Z}^+$, their positions $\mathbf{h}_i \in \mathbb{R}^3$, the matrix $\mathbf{A}_i \in \mathbb{R}^{6\times 6}$, and the orientation angles $\phi_i \in \mathbb{R}$. Treating these variables independently introduces significant complexity into the optimization process.

To mitigate this complexity, we adopt a structured approach by arranging the gimbal actuators in an evenly distributed star-shaped configuration. This symmetric configuration reduces the dimensionality of the design space, simplifies optimization, and ensures balanced force and torque distribution. Under this arrangement, the orientation angle ϕ_i of each sub-vehicle is:

$$\phi_i = \frac{2\pi(i-1)}{n}. \tag{17}$$

The position vectors $\mathbf{h}_i$ are derived by rotating a reference vector $\mathbf{h}_i$:

$$\mathbf{h}_i = \mathbf{R}_{Bi}^{B} \mathbf{h}_1, \tag{18}$$

where $\mathbf{R}_{Bi}^{B}$ is a rotation matrix derived from (1), $l_c = \|\mathbf{h}_i\| - r_c$, with $r_c \in \mathbb{R}^+$ denoting the radius of the central platform. Typically, r_c is determined by the payload mounting constraints.

Unlike the numerical optimization methods employed in previous research [23], these methods are not applicable to solving Problem 1. This is due to the discrete switching of passive joint types in matrix $\mathbf{A}$, which leads to discontinuity or non-differentiability in the objective function $\text{cond}(\mathbf{D})$. Specifically, matrix $\mathbf{A}$ is structured as a block diagonal matrix, where each diagonal block $\mathbf{A}_i$ encodes the force and torque constraints of passive joints, as defined in (6). Since the passive joint types in $\mathbf{A}$ are discrete—for instance, switching from a constrained passive joint to a single or dual-axis bearing joint—the diagonal elements α and β experience discrete jumps in value between different joint types.

This discrete switching of $\mathbf{A}$ results in abrupt changes in the singular values of the design matrix $\mathbf{D} = \mathbf{BRA}$. Consequently, the condition number of $\mathbf{D}$, defined as:

$$\text{cond}(\mathbf{D}) = \frac{\sigma_{\max}(\mathbf{D})}{\sigma_{\min}(\mathbf{D})}, \tag{19}$$

where $\sigma_{\max}(\mathbf{D})$ and $\sigma_{\min}(\mathbf{D})$ are the maximum and minimum singular values of $\mathbf{D}$, respectively, becomes discontinuous or non-differentiable when $\mathbf{A}$ is switched.

Furthermore, when changes in $\mathbf{A}$ cause $\mathbf{D}$ to approach singularity (i.e., $\sigma_{\min}(\mathbf{D}) \to 0$), the condition number $\text{cond}(\mathbf{D})$ tends to infinity, further exacerbating the discontinuity of the objective function. This poses challenges for optimization algorithms, such as gradient descent, as the lack of smoothness in the objective function can hinder stable convergence.

Therefore, we employ Algorithm 1 to find an optimal fully actuated design $\mathbb{D}_+$ that minimizes $\text{cond}(\mathbf{D})$. The algorithm systematically explores actuator counts $n \in [N_{\text{min}}, N_{\text{max}}]$ and joint matrix candidates $\mathbf{A}$ with $\text{rank}(\mathbf{A}) \ge 6$. For each candidate, we define the objective function $J(\mathbf{h}_1) = \text{cond}(\mathbf{D})$, with $\mathbf{h}_1$ as the optimization variable. Gradient descent is employed to update $\mathbf{h}_1$ while satisfying rank and length constraints. The optimization process iterates until the change in J falls below a predefined threshold $\epsilon \in \mathbb{R}^+$. Upon convergence, all $\mathbf{h}_i$ are computed via (17) and (18). If a lower condition number is achieved, cond_{min} is updated. The final output is the optimal design $\mathbb{D}_+$.

Algorithm 1 Optimization Design Algorithm for IAP

```
Input: $N_{min}, N_{max}, l_{min}, l_{max}, r_c$, initial position $\mathbf{h}_1^{(0)}$, convergence tolerance $\epsilon$, step size $\alpha$, maximum iterations $k_{\max}$.
Output: $\mathbb{D}_+ = (n, \mathbf{h}_1, ..., \mathbf{h}_n, \phi_i, \alpha_i, \beta_i)$.
Initialize cond$_{min} \leftarrow \infty$, $\mathbb{D}_+ \leftarrow \emptyset$.
for $n \leftarrow N_{min}$ to $N_{max}$ do
  for $\mathbf{A} \in \{\mathbf{A}^1, ..., \mathbf{A}^{4^n}\}$, with rank$(\mathbf{A}) \geq 6$ do
    Define $J(\mathbf{h}_1) = \text{cond}(\mathbf{D})$
    for $k = 1, 2, \ldots, k_{\max}$ do
      Update $\mathbf{h}_1^{(k+1)} \leftarrow \mathbf{h}_1^{(k)} - \alpha \nabla J$.
      Ensure constraints: adjust $\mathbf{h}_1$ if rank$(\mathbf{D}) < 6$ or $||\mathbf{h}_1|| < l_{\min} + r_c$ or $||\mathbf{h}_1|| > l_{\max} + r_c$.
      If $|J^{(k)} - J^{(k-1)}| < \epsilon$ then break.
    end for
    Compute $\{\mathbf{h}_i\}$ via (17) and (18).
    Construct $\mathbf{D}$ based on $n$, $\{\mathbf{h}_i\}$, $\mathbf{A}$.
    if cond$(\mathbf{D}) <$ cond$_{min}$ then
      Update cond$_{min} \leftarrow$ cond$(\mathbf{D})$.
      Update $\mathbb{D}_+ \leftarrow (n, \mathbf{A}, \mathbf{h}_1, \ldots, \mathbf{h}_n)$.
    end if
  end for
end for
return $\mathbb{D}_+$
```

IV. PROTOTYPE DESIGN AND CONTROL: TWO CASE STUDIES OF FULLY ACTUATED IAPS

A. Design of IAP Prototypes under Two Scenarios

In this section, provide two typical application scenarios for the IAP. The objective in each scenario is to determine the optimal configuration that minimizes the condition number of the design matrix under the given operational and physical constraints, thereby maximizing control performance and robustness.

1) IAP for Channel Navigation:

Scenario 1: Design an IAP configuration $\mathbb{D}_+^1$ that ensures full actuation and navigation through narrow passages of width 0.5 m. The IAP employs quadcopters with a 450 mm wheelbase as sub-vehicles, and the radius of the center platform is 0.15 m.

In Scenario 1, the IAP must navigate a 0.5 m-wide channel. To ensure the effective navigation while retaining full actuation, an in-line configuration with two sub-vehicles is adopted, leading to $N_{min} = N_{max} = 2$.

By executing Algorithm 1, an optimal design tuple $\mathbb{D}_+^1$ is obtained, resulting in a design matrix $\mathbf{D}_+^1$ with a condition number of 2.14. The algorithm is performed in MATLAB on an Intel i5 processor, with a computation time of approximately 146 seconds. The detailed parameters of $\mathbb{D}_+^1$ are summarized in Table II.

Based on the diagonal elements diag$(\mathbf{A}_1)^T$ and diag$(\mathbf{A}_2)^T$, a constrained passive joint is selected for sub-vehicle 1, and a spherical hinge joint is selected for sub-vehicle 2. The structural layout is illustrated in Fig. 2.

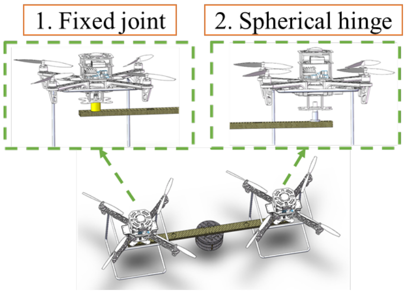

Fig. 2: IAP structure diagram of design $\mathbb{D}_+^1$.

TABLE II: Parameters for Design Tuples $\mathbb{D}_+^1$ and $\mathbb{D}_+^2$

Parameter	Value for $\mathbb{D}_+^1$	Value for $\mathbb{D}_+^2$
n	2	4
$\mathbf{h}_1$	[0.5, 0, -0.04]m	[0.22, 0.22, -0.04]m
$\mathbf{h}_2$	[-0.5, 0, -0.04]m	[-0.22, 0.22, -0.04]m
$\mathbf{h}_3$	–	[-0.22, -0.22, -0.04]m
$\mathbf{h}_4$	–	[0.22, -0.22, -0.04]m
diag$(\mathbf{A}_1)^T$	[0,0,1,1,1,1]	[1,1,1,0,0,0]
diag$(\mathbf{A}_2)^T$	[1,1,1,0,0,0]	[1,1,1,0,0,0]
diag$(\mathbf{A}_3)^T$	–	[1,1,1,0,0,0]
diag$(\mathbf{A}_4)^T$	–	[1,1,1,0,0,0]

2) IAP for Open-Area:

Scenario 2: For stable operation in open areas, a fully actuated $\mathbb{D}_+^2$ IAP is designed, incorporating quadrotor sub-vehicles (330 mm wheelbase). Key configuration constraints are: $n \leq 6$ (maximum sub-vehicles), $l_c \leq 0.5$ m (connection rod length), and a fixed central platform radius of 0.15 m.

To satisfy the scene requirements, l_{max} is set to 0.5 m. Due to the spatial constraints of l_{max} and the inter-axis distance of the sub-vehicles, N_{max} is set to 6. The minimum connecting rod length, l_{min}, is defined as 0.2 m, based on the sub-vehicle wheelbase.

Using Algorithm 1, the design optimization was conducted in MATLAB on an Intel i5 processor, completing in 312 seconds. The optimized design yielded a design matrix $\mathbf{D}_+^2$, with a condition number of 1.36. The corresponding design parameters are listed in Table II.

The diagonal entries of $\mathbf{A}_1$ to $\mathbf{A}_4$ indicate that all sub-vehicles in $\mathbb{D}_+^2$, are configured with spherical hinge joints. The design is illustrated in Fig. 3.

B. Pose Controller

The pose controller computes a reference force $\boldsymbol{f}_{B,r}$ and reference torque $\boldsymbol{\tau}_{B,r}$ based on the dynamics model introduced in (2):

$$\begin{cases} \boldsymbol{f}_{B,r} = m\dot{\boldsymbol{v}}_{B,r} + (m\boldsymbol{\omega}_B) \times \boldsymbol{v}_{B,r} - mg{\mathbf{R}_B^W}^T \mathbf{e}_3 \\ \qquad - \mathbf{K}_{pP}\mathbf{e}_p - \mathbf{K}_{pI}\int \mathbf{e}_p - \mathbf{K}_{pD}\dot{\mathbf{e}}_p, \\ \boldsymbol{\tau}_{B,r} = J\dot{\boldsymbol{\omega}}_{B,r} - (J\boldsymbol{\omega}_B) \times \boldsymbol{\omega}_{B,r} \\ \qquad - \mathbf{K}_{rP}\mathbf{e}_R - \mathbf{K}_{rI}\int \mathbf{e}_R - \mathbf{K}_{rD}\mathbf{e}_\omega, \end{cases} \tag{20}$$

where $\mathbf{e}_p = \mathbf{p}_{B,r} - \mathbf{p}_B \in \mathbb{R}^3$ is the position error, with $\mathbf{p}_{B,r}$ and $\mathbf{p}_B \in \mathbb{R}^3$ as the reference and actual position, respectively.

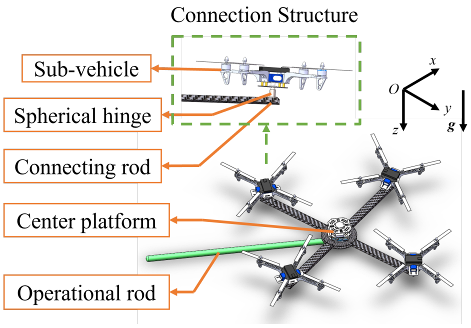

Fig. 3: IAP structure diagram of design $\mathbb{D}_+^2$.

$\mathbf{K}_{pP}, \mathbf{K}_{pI}, \mathbf{K}_{pD} \in \mathbb{R}^{3\times3}$ are the proportional, integral, and derivative (PID) control gains, applied independently along the x, y, and z axes. the attitude error $\mathbf{e}_R \in \mathbb{R}^3$ is given by $\mathbf{e}_R = \frac{1}{2}(\mathbf{R}_B^W \mathbf{R}_{B,r}^T - \mathbf{R}_B^{W^T} \mathbf{R}_{B,r})^\vee$, where $\mathbf{R}_{B,r} \in \mathbb{R}^{3\times3}$ is the reference rotation matrix. The operator $(\cdot)^\vee$ acts as the inverse of $(\cdot)^\wedge$, transforming a skew-symmetric matrix back into a 3D vector. And $\mathbf{e}_\omega$ is the angular velocity tracking error: $\mathbf{e}_\omega = \boldsymbol{\omega}_B - \mathbf{R}_B^{W^T} \mathbf{R}_{B,r} \boldsymbol{\omega}_{B,r}$, where $\boldsymbol{\omega}_{B,r} = (\mathbf{R}_{B,r}^T \dot{\mathbf{R}}_{B,r})^\vee \in \mathbb{R}^3$ is the reference angular velocity of the IAP. And $\mathbf{K}_{rP}, \mathbf{K}_{rI}, \mathbf{K}_{rD} \in \mathbb{R}^{3\times3}$ are the PID control gains for roll, pitch, and yaw, respectively.

C. Allocation Strategy

This section discusses the allocation strategy for solving the following problem:

Problem 2: Given a full rank design matrix $\mathbf{D} \in \mathbb{R}^{6\times 6n}$ and a desired control wrench $\mathbf{U} = [\boldsymbol{f}_{B,r}^T\ \boldsymbol{\tau}_{B,r}^T]^T \in \mathbb{R}^6$, determine the input $\mathbf{W}_d^{B1:Bn} \in \mathbb{R}^{6n}$.

A straightforward method to compute $\mathbf{W}_d^{B1:Bn}$ is through the Moore-Penrose pseudoinverse $\mathbf{D}^+ \in \mathbb{R}^{6\times6}$:

$$\mathbf{W}_d^{B1:Bn} = \mathbf{D}^+ \mathbf{U} + \mathbf{N}_D \mathbf{Z}, \tag{21}$$

where the matrix $\mathbf{N}_D \in \mathbb{R}^{6n\times6}$ represents a basis for the nullspace of $\mathbf{D}$, capturing the free space in actuation. $\mathbf{Z} \in \mathbb{R}^6$ is an arbitrary vector. It is seen that setting $\mathbf{Z} = 0$ yields the least-squares solution that minimizes control effort [24].

This approach uses a straightforward computational process suitable for high-frequency controller sampling, ensuring real-time performance. It applies the least squares method to optimize the solution from (10), minimizing controller output and enhancing energy efficiency.

1) Prototype IAP design $\mathbb{D}_+^1$: The desired total wrench for IAP is given by:

$$\mathbf{U}_1 = \mathbf{D}_+^1 \begin{bmatrix} \mathbf{W}_1^{B1} \\ \mathbf{W}_2^{B2} \end{bmatrix}. \tag{22}$$

It is allocated to the sub-vehicles using the design matrix $\mathbb{D}_+^1$. $\mathbf{W}_1^{B1} \in \mathbb{R}^6$ and $\mathbf{W}_2^{B2} \in \mathbb{R}^6$ are the local wrenches allocated to the two sub-vehicle.

Sub-vehicle 1 is connected by a constrained passive joint, allowing it to exert thrust along its z-axis and generate torques around all three axes. The allocated wrench is constrained to $\mathbf{W}_1^{B1} = \mathbf{W}_1^{s1} = [0\ 0\ T_1\ \tau_1^x\ \tau_1^y\ \tau_1^z]^T$. Thus, the corresponding command sent to its onboard flight controller is $\mathbf{u}_{d1} = [T_1\ \tau_1^x\ \tau_1^y\ \tau_1^z]^T$.

Sub-vehicle 2 is attached via a spherical joint, which cannot transmit torque. Thus, the allocated wrench is: $\mathbf{W}_2^{B2} = [\boldsymbol{f}_2^{B2}; \mathbf{0}_{3\times1}]$, where the desired force $\boldsymbol{f}_2^{Bi} \in \mathbb{R}^3$ is computed from the desired thrust direction and magnitude:

$$\boldsymbol{f}_2^{B2} = (\mathbf{R}_B^W \mathbf{R}_{B2}^B)^T \mathbf{R}_{d2}^W T_2 \mathbf{e}_3. \tag{23}$$

Here, T_2 represents the required thrust, and $\mathbf{R}_{d2}^W \in \mathbb{R}^{3\times3}$ denotes the desired orientation. The reference commands T_2 and $\mathbf{R}_{d2}^W$ are sent to the attitude controller of sub-vehicle 2 to compute the final control command, which is given by $\mathbf{u}_{d2} = [T_2\ \tau_2^x\ \tau_2^y\ \tau_2^z]^T$.

For sub-vehicle's attitude controller design, we refer to existing frameworks such as [25].

2) Prototype IAP design $\mathbb{D}_+^2$: The use of spherical joints decouples the orientation of sub-vehicles from the central platform, allowing the sub-vehicles to act as force generators.

Let $\Lambda_i = [f_i^x; f_i^y; f_i^z] \in \mathbb{R}^3$ denotes the force applied by sub-vehicle i in its local body frame $\{\mathcal{F}_{si}\}$, the total wrench $\mathbf{U}_2 \in \mathbb{R}^6$ applied to the platform can be obtained as:

$$\mathbf{U}_2 = \mathbf{D}_+^2 \begin{bmatrix} \Lambda_1 & \Lambda_2 & \Lambda_3 & \Lambda_4 \end{bmatrix}^T, \tag{24}$$

where the *design matrix* $\mathbf{D}_+^2 \in \mathbb{R}^{6\times24}$ is given by:

$$\mathbf{D}_+^2 = \begin{bmatrix} \mathbf{I}_{3\times3} & \mathbf{I}_{3\times3} & \mathbf{I}_{3\times3} & \mathbf{I}_{3\times3} \\ \mathbf{h}_1^\wedge & \mathbf{h}_2^\wedge & \mathbf{h}_3^\wedge & \mathbf{h}_4^\wedge \end{bmatrix}. \tag{25}$$

The force allocation is computed using the allocation strategy outlined in Section IV-C. Each resulting thrust vector $\Lambda_i \in \mathbb{R}^3$ is converted into a thrust magnitude and desired orientation using (23), which are passed to the sub-vehicles' attitude controller.

V. SIMULATION AND EXPERIMENTAL VALIDATION

A. Wrench Variation Comparison

To evaluate the control stability of different IAP designs, we compare the optimal design $\mathbb{D}_+^2$ with a suboptimal variant $\mathbb{D}_+^{2s}$, both subject to the same constraints (Scenario 2). The condition number of the design matrix corresponding to $\mathbb{D}_+^{2s}$ is $\text{cond}(\mathbf{D}_+^{2s}) = 1.90$. For further comparison, the prototype platform $\mathbf{D}_3^+$, which comprises four submodules each equipped with double-bearing passive joints [10], has a design matrix condition number of $\text{cond}(\mathbf{D}_3^+) = 2.11$.

Let $\mathbf{W}^j \in \mathbb{R}^6$ denote the control wrench at the j-th control period. The amount of wrench variation in each control wrench is expressed in terms of the Euclidean distance:

$$\Delta_d^j = \|\mathbf{W}_d^j - \mathbf{W}_d^{j-1}\|_2. \tag{26}$$

This metric captures the wrench fluctuation between consecutive control periods.

As illustrated in Fig. 4, the optimal design $\mathbb{D}_+^2$ consistently yields lower values of Δ_d^j throughout the entire control cycle. This outcome corroborates the effectiveness of our optimization criterion, indicating that minimizing the condition number reduces variations in control effort, thereby improving both system stability and energy efficiency.

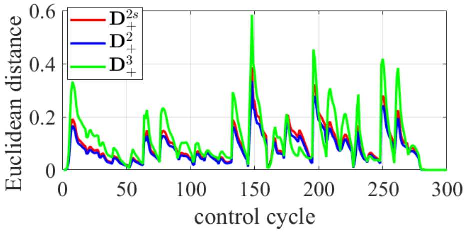

Fig. 4: For design matrices $\mathbf{D}^2_+$, $\mathbf{D}^{2s}_+$ and $\mathbf{D}^3_+$, the Euclidean distance curve of the output wrench across adjacent control cycles is provided for the same sequence of control wrenches $\{\mathbf{W}^1 \dots \mathbf{W}^j\}$.

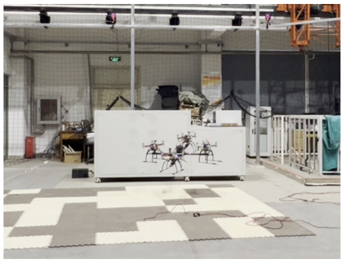

Fig. 5: IAP prototype for Scenario 2 ($\mathbb{D}^2_+$) hovering at an tilted angle.

B. *Simulation Experiment of $\mathbb{D}^1_+$*

To validate the full actuation of design $\mathbb{D}^1_+$, pose tracking experiments were conducted in Simulink using a coupled 3D position and attitude reference trajectory.

As shown in Fig. 6, the $\mathbb{D}^1_+$ IAP accurately tracks a coupled 3D position and attitude reference trajectory, including tilted hover. This simulation, depicted in Fig. 6-(a) and (b), unequivocally demonstrates the full actuation capability of the $\mathbb{D}^1_+$ design. This experimant validates the completeness of our optimal design framework, showcasing its ability to handle and optimize complex IAP systems with mixed joint types.

C. *Real-World Flight Test of $\mathbb{D}^2_+$*

The four-actuator design of $\mathbb{D}^2_+$ for open area was evaluated through outdoor flight experiments.

The IAP tracks both position and attitude references simultaneously, maintaining full pose control in real-world settings. As shown in Fig. 5, the platform achieves stable hovering under a tilted attitude. The tracking results presented in Fig. 7-(a) and Fig. 7-(b) indicate that the attitude tracking remains within 5°, and the position tracking error is below 0.4 m. These results demonstrate the effectiveness of the optimized design $\mathbb{D}^2_+$ as a fully actuated platform.

D. *Real-World Experiments On Direct Wrench Control Contacts for $\mathbb{D}^2_+$ IAP*

To demonstrate the benefits of IAP for contact-based operations compared to underactuated flying platforms, we developed a 6-DOF force/torque interaction controller utilizing a hybrid force/position control strategy. The detailed methodology for this controller's design is provided in [19].

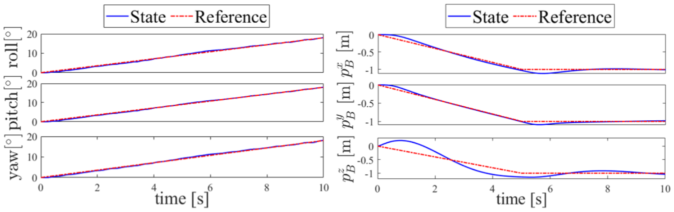

(a) Attitude tracking result.
(b) Position tracking result.

Fig. 6: Simulation attitude and position tracking result of prototype $\mathbb{D}^1_+$ design IAP.

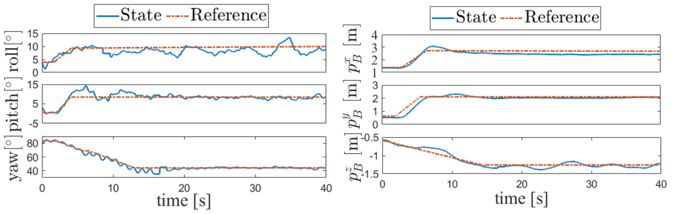

(a) Attitude tracking result.
(b) Position tracking result.

Fig. 7: Attitude and position tracking result of prototype $\mathbb{D}^2_+$ designed IAP.

The IAP, designed within the $\mathbb{D}^2_+$, is equipped with a linkage arm extending along the negative x-axis of the body frame $\mathcal{F}_B$. The distal end of this linkage features a rough contact surface measuring $10\,\mathrm{cm} \times 10\,\mathrm{cm}$, as illustrated in Fig. 8. During interaction with a static environment (the ground), the IAP dynamically adjusts its attitude while maintaining a reference force of $20\,\mathrm{N}$ along the $\mathcal{F}^x_B$ axis, with all other forces and torques constrained to zero. By subjecting the external environment to independently applied forces and torques, we experimentally validate the IAP's superior capability in performing contact tasks—capabilities unattainable by conventional under-actuated aerial platforms. The corresponding pose tracking and force/torque tracking results under direct wrench control are presented in Fig. 9 and 10.

VI. DISCUSSION

This paper considers only four simple types of passive joints and develops an optimized design algorithm specifically tailored to these joint types. Future work will extend this framework to incorporate more complex passive joints. Regarding the solver for the optimization algorithm, the computational complexity increases significantly with the number of submodules, thus motivating future efforts to improve the algorithm's time efficiency. In terms of disturbance rejection, the IAP enhances robustness and fault tolerance by employing a carefully tuned motion controller alongside an optimized design matrix characterized by a low condition number. This approach effectively minimizes fluctuations in control effort, thereby improving both system stability and energy efficiency.

VII. CONCLUSION

In this paper, we introduce a novel optimization framework for the design of IAP that incorporates various passive

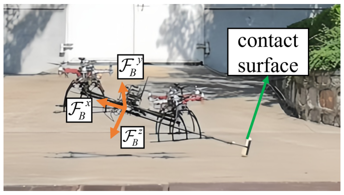

Fig. 8: The direct wrench control experiments of the IAP prototype for Scenario 2 ($\mathbb{D}_+^2$).

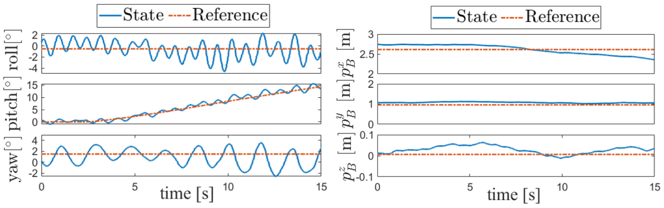

(a) Attitude tracking result. (b) Position tracking result.

Fig. 9: Direct wrench control experiment pose tracking result of prototype $\mathbb{D}_+^2$ designed IAP.

joint types. By establishing the necessary conditions for full actuation, the proposed approach enables systematic selection of sub-vehicle configurations and joint types. The optimization objective minimizes the condition number of the design matrix, enhancing both control performance and stability. The proposed method is validated through simulations and real-world flight tests across multiple scenarios. These results demonstrate the practical effectiveness and offer actionable insights for IAP platform design and optimization.

REFERENCES

[1] S. C. Barakou, C. S. Tzafestas, and K. P. Valavanis, "Real-time applicable cooperative aerial manipulation: A survey," in *2023 International Conference on Unmanned Aircraft Systems (ICUAS)*, 2023, pp. 634–643.

[2] J. Welde and V. Kumar, "Coordinate-free dynamics and differential flatness of a class of 6dof aerial manipulators," in *2020 IEEE International Conference on Robotics and Automation (ICRA)*, 2020, pp. 4307–4313.

[3] M. Faessler, F. Fontana, C. Forster, E. Mueggler, M. Pizzoli, and D. Scaramuzza, "Autonomous, vision-based flight and live dense 3d mapping with a quadrotor micro aerial vehicle," *Journal of Field Robotics*, vol. 33, no. 4, pp. 431–450, 2016.

[4] Y. Yu and X. Ding, "Safe landing analysis of a quadrotor aircraft with two legs," *Journal of Intelligent & Robotic Systems*, vol. 76, pp. 527–537, 2014.

[5] M. Tognon and A. Franchi, "Dynamics, control, and estimation for aerial robots tethered by cables or bars," *IEEE Transactions on Robotics*, vol. PP, 03 2016.

[6] B. Yueksel, C. Secchi, and A. Franchi, "Aerial physical interaction via reshaping of the physical properties: Passivity-based control methods and nonlinear force observers," 05 2014.

[7] B. Mu and P. Chirarattananon, "Universal flying objects: Modular multirotor system for flight of rigid objects," *IEEE Transactions on Robotics*, vol. 36, no. 2, pp. 458–471, 2020.

[8] K. Oishi and T. Jimbo, "Autonomous cooperative transportation system involving multi-aerial robots with variable attachment mechanism," in *2021 IEEE/RSJ International Conference on Intelligent Robots and Systems (IROS)*, 2021, pp. 6322–6328.

[9] C. Bosio and M. W. Mueller, "Automated layout and control co-design of robust multi-uav transportation systems," *IEEE Robotics and Automation Letters*, vol. 10, no. 4, pp. 3956–3963, 2025.

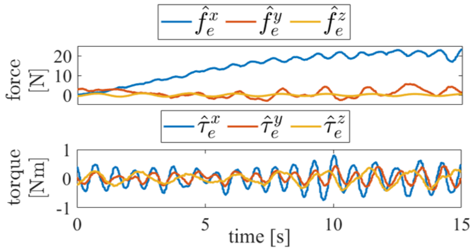

Fig. 10: The direct wrench control experiments force and torque tracking result of prototype $\mathbb{D}_+^2$ designed IAP.

[10] P. Yu, Y. Su, M. J. Gerber, L. Ruan, and T.-C. Tsao, "An over-actuated multi-rotor aerial vehicle with unconstrained attitude angles and high thrust efficiencies," *IEEE Robotics and Automation Letters*, vol. 6, no. 4, pp. 6828–6835, 2021.

[11] M. Ryll, D. Bicego, M. Giurato, M. Lovera, and A. Franchi, "Fast-hex—a morphing hexarotor: Design, mechanical implementation, control and experimental validation," *IEEE/ASME Transactions on Mechatronics*, vol. 27, no. 3, pp. 1244–1255, 2022.

[12] S. J. Lee, D. Lee, J. Kim, D. Kim, I. Jang, and H. J. Kim, "Fully actuated autonomous flight of thruster-tilting multirotor," *IEEE/ASME Transactions on Mechatronics*, vol. 26, no. 2, pp. 765–776, 2021.

[13] G. Loianno and V. Kumar, "Cooperative Transportation Using Small Quadrotors Using Monocular Vision and Inertial Sensing," *IEEE Robot. Autom. Lett.*, vol. 3, no. 2, pp. 680–687, Apr. 2018.

[14] L. Ruan, *Independent position and attitude control on multirotor aerial platforms*. University of California, Los Angeles, 2020.

[15] J. Sun, K. Wang, C. Shi, X. Li, X. Yi, Y. Yu, F. Sun, and Y. Dong, "Modeling and control of PADUAV: a passively articulated dual UAVs platform for aerial manipulation*," in *2024 IEEE International Conference on Robotics and Automation (ICRA)*. IEEE, pp. 6159–6165. [Online]. Available: https://ieeexplore.ieee.org/document/10610094/

[16] H.-N. Nguyen, S. Park, J. Park, and D. Lee, "A novel robotic platform for aerial manipulation using quadrotors as rotating thrust generators," *IEEE Transactions on Robotics*, vol. 34, no. 2, pp. 353–369, 2018.

[17] C. Shi, K. Wang, and Y. Yu, "Expandable fully actuated aerial vehicle assembly: Geometric control adapted from an existing flight controller and real-world prototype implementation," *Drones*, vol. 6, no. 10, p. 272, 2022.

[18] J. Sugihara, M. Zhao, T. Nishio, K. Okada, and M. Inaba, "BEATLE - Self-Reconfigurable Aerial Robot: Design, Control and Experimental Validation," Apr. 2024, arXiv:2404.09153 [cs].

[19] K. Wang, G. Lai, Y. Yu, J. Du, J. Sun, B. Xu, A. Franchi, and F. Sun, "Versatile tasks on integrated aerial platforms using only onboard sensors: Control, estimation, and validation," *IEEE Transactions on Robotics*, vol. 41, pp. 3518–3538, 2025.

[20] Y. Su, Z. Jiao, Z. Zhang, J. Zhang, H. Li, M. Wang, and H. Liu, "Flight structure optimization of modular reconfigurable uavs," 2024. [Online]. Available: https://arxiv.org/abs/2407.03724

[21] D. Saldaña, P. M. Gupta, and V. Kumar, "Design and control of aerial modules for inflight self-disassembly," *IEEE Robotics and Automation Letters*, vol. 4, no. 4, pp. 3410–3417, 2019.

[22] J. Du, K. Wang, Y. Fan, G. Lai, and Y. Yu, "High-fidelity integrated aerial platform simulation for control, perception, and learning," *IEEE Transactions on Automation Science and Engineering*, pp. 1–1, 2025.

[23] M. Tognon and A. Franchi, "Omnidirectional Aerial Vehicles With Unidirectional Thrusters: Theory, Optimal Design, and Control," *IEEE Robotics and Automation Letters*, vol. 3, no. 3, pp. 2277–2282, Jul. 2018. [Online]. Available: http://ieeexplore.ieee.org/document/8281444/

[24] Y. Su, P. Yu, M. J. Gerber, L. Ruan, and T.-C. Tsao, "Nullspace-based control allocation of overactuated UAV platforms," vol. 6, no. 4, pp. 8094–8101. [Online]. Available: https://ieeexplore.ieee.org/document/9511202/

[25] C. Shi, G. Lai, Y. Yu, M. Bellone, and V. Lippiello, "Real-time multi-modal active vision for object detection on uavs equipped with limited field of view lidar and camera," *IEEE Robotics and Automation Letters*, vol. 8, no. 10, pp. 6571–6578, 2023.